J Mater Sci (2007) 42:9894–9904
DOI 10.1007/s10853-006-1479-4

Experimental and theoretical investigation of nonlinear viscoelastic polyurethane systems

Michael Johlitz · Holger Steeb · Stefan Diebels · Anthippi Chatzouridou · Jan Batal · Wulff Possart

Received: 18 July 2006 / Accepted: 21 December 2006 / Published online: 20 August 2007

Abstract The non-linear viscoelastic behaviour of a polyurethane (PUR) network is determined by continuous uniaxial tension tests and stepwise relaxation tests. Following the concept of internal variables on the modelling side, the finite Neo-Hookean material model combined with linear evolution equations for the internal variables is applied to include the time-dependence caused by viscoelasticity. The parameters are identified by an evolution strategy combined with a non-linear finite element analysis which solves the boundary value problem given by the specimen geometry and testing conditions. In conclusion, the combination of the described experiments and modelling provides a full description of the mechanical behaviour of the given PUR.

Introduction and motivation

Polymers are widely used as adhesives in industrial applications, i.e. in automotive and aeronautical engineering. The appropriate description of the mechanical behaviour of such adhesive joints still poses a variety of problems, i.e. very often the mechanical properties of the viscoelastic polymer are not known with necessary precision. This is the motivation for our current research project which deals with the modelling of polymer joints under quasi-static and, at first, isothermal conditions at ambient temperature (RT). Before analysing the complexity of an adhesive in the joint, the bulk material itself is studied in detail in this paper. Therefore, we prepare tensile specimens which are investigated in our custom-made high precision tensile tester GALLUS (proper name) [4, 5]. Experiments are performed either with constant tensile strain rate or as stress relaxation measurements at given strain levels for finite deformations.

Many publications concerning polyurethanes like [14, 41] focus on the influence of its components and their concentration on mechanical behaviour without modelling the viscoelasticity. Others like [27, 40] adapt one-dimensional rheological models to experimental data obtained from small deformation tests. Sophisticated continuum mechanical models are discussed, e.g. by Khan et al. [21] and Lion [31] for polyurethane based rubbers and filled elastomers, respectively. Nevertheless, for the particular used reactive PUR system no appropriate mechanical characterisation is reported in literature. Moreover, the mechanical properties of a PUR network are sensitive to the route of chemical processing. Therefore, literature data would not have the reliability needed for our study.

Finally, the goal of this contribution is to recall the possibilities of continuum mechanical modelling applied to viscoelastic solids and to fit such a model to data obtained from experimental investigations. In the limits of our experimental investigations the PUR possesses a typical viscoelastic behaviour of a solid without any plasticity or damage (i.e. Mullins effect). Furthermore, the material proves to be incompressible. For the relaxed solid the elasticity can be described by the Neo-Hookean law [38, 48, 52]. From the constitutive point of view, this incompressible Neo-Hookean material model is combined with

M. Johlitz · H. Steeb (✉) · S. Diebels · A. Chatzouridou
Chair of Applied Mechanics, Saarland University, D-66041 Saarbrücken, Germany
e-mail: h.steeb@mx.uni-saarland.de

J. Batal · W. Possart
Chair of Adhesion and Interphases in Polymers, Saarland University, D-66041 Saarbrücken, Germany

linear evolution equations for the internal variables allowing to prescribe the viscoelastic response of the polyurethane in a convenient manner, i.e. the relaxation behaviour is described by a number of relaxation times. The parameters of that material model are determined by an evolution strategy which provides the parameter data on the basis of the measured tensile test curves.

Modelling aspects

In our contribution we restrict ourselves to isothermal conditions. At first, the basic idea of the formulation for viscoelastic solids is briefly revisualised. The initial point of the continuum mechanical considerations is a rheological model as shown in Fig. 1. An extra spring element is connected in parallel with $j = 1,...,n$ spring-dashpot elements (Maxwell elements). As the extra spring represents the elasticity in the relaxed state, the Maxwell elements reproduce the viscoelastic component of the material response.

The realisation of the finite viscoelasticity is based on the concept of deformation-valued internal variables as published by Reese [43–47], Lubliner [32], Le Tallec [51], Lion [28–30], Haupt [19, 20], Amin [1–3], Boyce and others [8–11, 22, 34–37]. We consider the same Neo-Hookean modelling approach for all springs, and the dashpots are represented by a linear viscous approach. Any sophisticated viscoelastic behaviour can be described using a sufficient number of Maxwell elements. Typically one or two Maxwell elements are sufficient to describe the relaxation response per decade of time.

The deformation of the extra spring, i.e. the basic elasticity, is described by the left Cauchy-Green deformation tensor $\mathbf{B} = \mathbf{F}\cdot\mathbf{F}^T$ which is a measure of the current configuration $\mathcal{B}$.

Starting from the multiplicative decomposition of the deformation gradient $\mathbf{F}$ into an elastic and an inelastic part $\mathbf{F}_e$ and $\mathbf{F}_i$, respectively, a fictive intermediate configuration $\mathcal{B}_i$ for each Maxwell element is established:

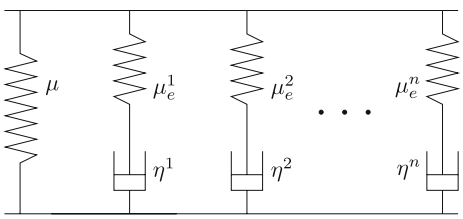

Fig. 1 Rheological model of the viscoelasticity with $j = 1,...,n$ Maxwell elements

$$\mathbf{F} = \mathbf{F}_e^j \cdot \mathbf{F}_i^j. \tag{1}$$

The multiplicative decomposition is developed and motivated in the context of plasticity of crystals [23, 25, 26]. In the context of finite viscoelasticity it is used as a constitutive assumption [43]. Bergström and Boyce [7] interpreted the intermediate configuration as stress-free, i.e. the non-equilibrium stress is assumed to be locally completely relaxed. Thus, one obtains deformation and stress measures with respect to the reference configuration $\mathcal{B}_0$, intermediate configuration $\mathcal{B}_i$ and current configuration $\mathcal{B}$,

$$\mathbf{C}_i^j := \mathbf{F}_i^{jT} \cdot \mathbf{F}_i^j \text{ and } \mathbf{B}_e^j := \mathbf{F}_e^j \cdot \mathbf{F}_e^{jT}. \tag{2}$$

The second order deformation tensors $\mathbf{C}_i^j, j = 1,...,n$, describe the inelastic deformation of the n dashpots of all Maxwell elements with respect to the reference configuration $\mathcal{B}_0$, while the tensors $\mathbf{B}_e^j$ describe the elastic deformation of the springs in the Maxwell elements with respect to the current configuration $\mathcal{B}$. The following relationship can be derived between the deformation tensors $\mathbf{C}_i^j$ and $\mathbf{B}_e^j$:

$$\mathbf{B}_e^j = \mathbf{F} \cdot (\mathbf{C}_i^j)^{-1} \cdot \mathbf{F}^T. \tag{3}$$

For detailed discussion of the kinematic quantities, see e.g. [18, 43, 45, 3]. The derivation of the stress-deformation relation follows by the evaluation of the entropy principle in the form of the Clausius-Planck-inequality for the isothermal case [18]:

$$-\rho\dot{\Psi} + \mathbf{T} : \mathbf{D} \geq 0. \tag{4}$$

Herein **T:D** stands for the stress power defined by the Cauchy stress tensor $\mathbf{T}$ and the deformation rate $\mathbf{D}$. For the derivation of the Clausius-Planck-inequality the Helmholtz free energy density $\Psi = \varepsilon - \eta T$ is defined in the form of the Legendre transformation between the internal energy density ε, the entropy density η and the absolute temperature T.

Based on the choice of the process variables, the free energy density function Ψ is split into a purely elastic part and a viscoelastic part of the material behaviour, the so-called non-equilibrium part [43]

$$\Psi = \Psi_{eq}(\mathbf{B}) + \sum_{j=1}^{n} \Psi_{neq}^j(\mathbf{B}_e^j). \tag{5}$$

Note that the equilibrium part only depends on the deformation $\mathbf{B}$ while the non-equilibrium parts depend on the elastic deformation of the springs in the individual Maxwell elements, i.e. on $\mathbf{B}_e^j$. The time-based development of the non-equilibrium part is described by an evolution equation according to the Clausius-Planck inequality. For the internal variables we choose the tensors $\mathbf{C}_i^j$ with respect

to the reference configuration $\mathcal{B}_0$. After some calculations one obtains the Clausius-Planck inequality in the form

$$\left(\mathbf{T}+p\mathbf{I}-2\rho\mathbf{B}\cdot\frac{\partial\Psi_{eq}}{\partial\mathbf{B}}-\sum_{j=1}^{n}2\rho\mathbf{B}_e^j\cdot\frac{\partial\Psi_{neq}}{\partial\mathbf{B}_e^j}\right):\mathbf{D}-\sum_{j=1}^{n}\rho\frac{\partial\Psi_{neq}^j}{\partial\mathbf{C}_i^j}:\dot{\mathbf{C}}_i^j\geq 0. \tag{6}$$

In this context the Lagrange parameter p in combination with the constraint div $\mathbf{v} = 0$ was added to the balance of entropy describing the unknown pressure of the incompressible material. Executing the evaluation of the entropy principle according to the classical argumentation of Coleman and Noll [12] one obtains the Cauchy stress tensor

$$\mathbf{T}=-p\mathbf{I}+\mathbf{T}_{eq}+\sum_{j=1}^{n}\mathbf{T}_{neq}^j. \tag{7}$$

The equilibrium stress and the non-equilibrium stresses of the springs of the Maxwell elements $j = 1,...,n$ are described by the same Neo-Hookean [48] approach

$$\mathbf{T}_{eq}=\mu\mathbf{B}\ \text{and}\ \mathbf{T}_{neq}^j=\mu_e^j\mathbf{B}_e^j, \tag{8}$$

respectively. In this context the parameter μ stands for the shear modulus of the material in the relaxed state and the μ_e^j represent the shear moduli of the springs in the Maxwell elements.

As can be shown [43, 45], linear evolution equations

$$\dot{\mathbf{C}}_i^j=\frac{1}{r^j}\left(\mathbf{C}-\mathbf{C}_i^j\right) \tag{9}$$

formulated with respect to the reference configuration $\mathcal{B}_0$ satisfy the Clausius-Planck inequality 6. The second order tensor $\mathbf{C} = \mathbf{F}^T\cdot\mathbf{F}$ is the right Cauchy-Green deformation tensor. The 2 n parameters μ_e^j and r^j are the additional viscoelastic material parameters which are investigated by uniaxial tension experiments under constant strain rates. Here, $r^j = \eta^j/\mu^j$ stands for the relaxation time and describes the exponential decay of the stresses in the individual Maxwell element in relaxation experiments. Equation 9 describes the behaviour of deformation of the dashpot elements with respect to the deformation of the complete model and of the time.

In the numerical solution scheme, the evolution equations themselves are solved by an implicit backward-Euler integration scheme. Starting from the basic approach for a time-dependent variable one obtains the equation

$$\mathbf{C}_i^j(t_{n+1})=\frac{\Delta t}{r^j+\Delta t}\mathbf{C}(t_{n+1})+\frac{r^j}{r^j+\Delta t}\mathbf{C}_i^j(t_n). \tag{10}$$

This equation has to be solved for each Maxwell element and for each time step $\Delta t = t_{n+1} - t_n$ at each integration point of the finite element calculation. Note in passing that any other integration scheme can be applied, e.g. Runge–Kutta schemes [13, 16].

In the frame of the finite element analysis, the balance of momentum and the incompressibility constraint are treated in combination with the constitutive Eqs. 7–9. Starting from the equilibrium and the incompressibility constraint in the strong form

$$\operatorname{div}\mathbf{T}=\mathbf{0},\qquad \det\mathbf{F}-1=0, \tag{11}$$

the weak form of the saddle-point problem is derived by multiplication with the test functions $\delta\mathbf{u}$ and δp and by integration by parts over the domain of $\mathcal{B}$

$$\begin{aligned}\int_{\mathcal{B}}\mathbf{T}:\operatorname{grad}\delta\mathbf{u}\,dv&=\int_{\partial\mathcal{B}}\bar{\mathbf{t}}\cdot\delta\mathbf{u}\,da,\\ \int_{\mathcal{B}}(\det\mathbf{F}-1)\delta p\,dv&=0.\end{aligned} \tag{12}$$

For the displacement $\mathbf{u}$, Dirichlet- and Neumann-boundary conditions can be prescribed on the boundary $\Gamma = \partial\mathcal{B}$ with $\Gamma_D \cup \Gamma_N = \Gamma$ to $\mathbf{u} = \bar{\mathbf{u}}$ on Γ_D and $\mathbf{t} = \bar{\mathbf{t}}$ on Γ_N. From the numerical point of view we apply a mixed Taylor-Hood-like element formulation as shown in Fig. 2 which is known to be stable and reliable, cf. Braess [6]. The mixed element formulation in the form of Eq. 12 is implemented into the research code PANDAS, cf. [15], in addition to the discrete evolution Eq. 10 and the constitutive Eqs. 8.

Specimen preparation and experimental setup

Preparation of the samples

The investigated polyurethane network is synthesised from three commercial monomers of the Bayer AG.

– Desmodur®CD: 89% diphenylmethane-4,4-diisocyanate and 11% urethoneimine triisocyanate (inhibitor of crystallisation). Concerning this modification, Desmodur®CD is also called modified diisocyanate, or shortly MDI (see Fig. 3 for MDI as the principal component)

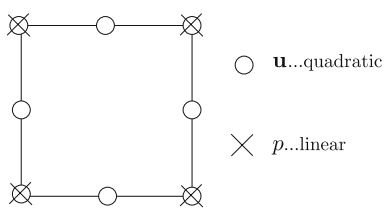

Fig. 2 Nodal points and unknowns of the mixed Q2P1 element

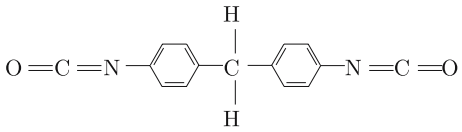

Fig. 3 Diphenylmethane-4,4-diisocyanate (MDI)

- Desmophen®2060 BD: linear polypropylene ether diol, shortly diol, chemical structure, see Fig. 4.
- Desmophen®1380 BT: polypropylene ether triol, shortly triol, chemical structure, see Fig. 5.

The chemical reaction of Desmophen®2060 BD with MDI results in linear chains, while Desmophen®1380 BT contributes cross-links for its trifunctionality. Hence, the mechanical behaviour of the polymer can be adjusted by variations of the mixing ratio of triol and diol. Here we use a mixture with the ratios $OH_{Triol} : OH_{Diol} = 4 : 1$ and $OH_{total} : NCO = 1 : 1$.

The monomers are stored and mixed in desiccated air at room temperature within a glove box to avoid parasitic reactions of the isocyanate with water. After thorough stirring of the components, the mixture is vacuum-degassed at 2 torr for 10 min to make the resulting polymer free of gas bubbles. Testing this step with the single components, no significant mass loss was detected.

For the preparation of the dogbone specimens (Fig. 6), the reacting monomer mixture is cast on a levelled PTFE surface within the glove box where it forms a film of 1.5 mm thickness. It is cross-linked at room temperature for 72 h and then fully cured in dried air at 90 °C for another four hours.

The specimens are die cut from the film. One film made out of 97 g of PUR yields approximately 30 dogbone specimens which have a length of 75 mm, a width of 4 mm in the centre of the dogbone and a film thickness of approximately 1.5 mm. All samples are numbered and the thickness, width and length are measured. This material has a glass transition temperature of $T_g \approx 0$ °C as measured by differential scanning caliometry (DSC) experiments at 10 K/min heating rate in nitrogen atmosphere. Hence, this PUR is an ideal prototype for elastomer polymers in the viscoelastic state. For optical measurements of deformation in the tensile tests, the dogbone specimens are patterned via a physical vapour deposition (PVD) process with 100 nm thick and 0.5 mm wide horizontal aluminium stripes. Due to their small thickness the aluminium stripes do not influence the mechanical behaviour of the PUR samples.

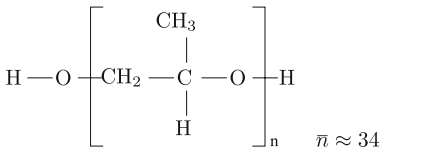

Fig. 4 Polpropylene ether diol, $\bar{n} \widehat{=}$ average degree of polymerisation

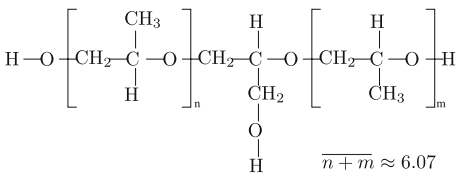

Fig. 5 Polypropylene ether triol, $\overline{n+m} \widehat{=}$ average degree of polymerisation

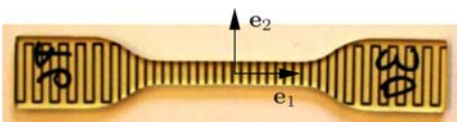

Fig. 6 Dogbone specimen (ISO 527-2:1996 type 5A) evaporated with Al stripes

Description of the tensile tester

The displacement controlled tensile tester GALLUS is custom-made with a force range of $F = \pm 20$ N at a resolution of 5 mN. The schematic view of the machine is shown in Fig. 7. It covers a displacement range of 50 mm in the $\mathbf{e}_1$-axis (cf. Figs. 6 and 7) at a resolution of 1 µm.

The specimens are fixed on both sides with a custom-made retention system and the expansion during the tensile

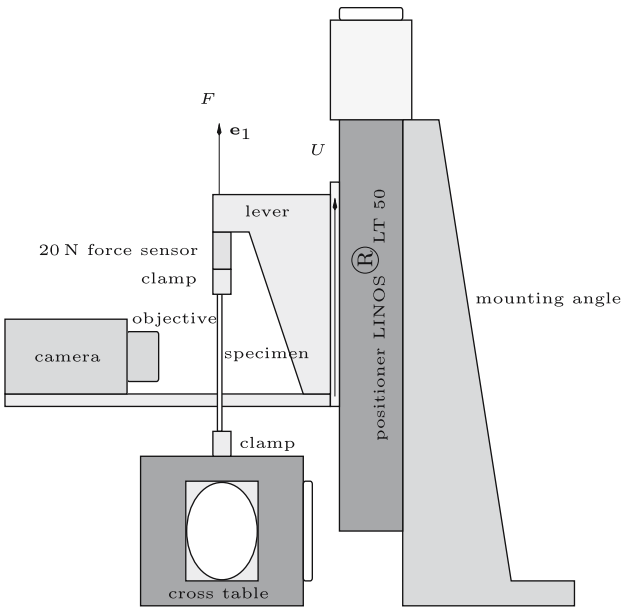

Fig. 7 Experimental setup for the uniaxial tension test

tests is applied by the path controlled vertical positioner LINOS®LT 50. During the measurement the transparent samples are illuminated from behind to give a good contrast of the aluminium stripes. The displacement of these stripes is detected by a high-resolution CCD camera for video extensiometry.

The video analysis is carried out with a NI Vision Development System® using pattern recognition to find the edges of the aluminium stripes from which we calculate the stretches in longitudinal $\mathbf{e}_1$-direction and in cross direction $\mathbf{e}_2$, respectively. Direct measurement of the displacement field renders the machine stiffness negligible. Nevertheless, we tested it by substituting the sample by a piece of high grade steel and found an overall linear machine deformation of 2.8 μm/N. This corresponds to a few parts per thousand of the sample deformation within the calibrated force range.

Experimental and mathematical investigation concerning the pure elastic behaviour of the PUR

Preliminary tests have shown that the investigated polyurethane has an average fracture deformation of about 80–90%. Hence, we restrict the measurement to a maximum deformation of 60%. Up to this state, damage can be excluded as proven by repeated loading-unloading experiments. Now it will be shown that the Neo-Hookean material model is appropriate to model PUR.

In the first step of modelling we take only the pure elastic behaviour into account. The pure elasticity is derived from uniaxial tension tests performed on our testing device GALLUS. Here, the sample elongation is stopped at a series of points and then the sample is allowed to relax. Figure 8 shows this discontinuous tension test for a holding time of about 180 s and a deformation step of 1 mm elongation (machine displacement) per load step.

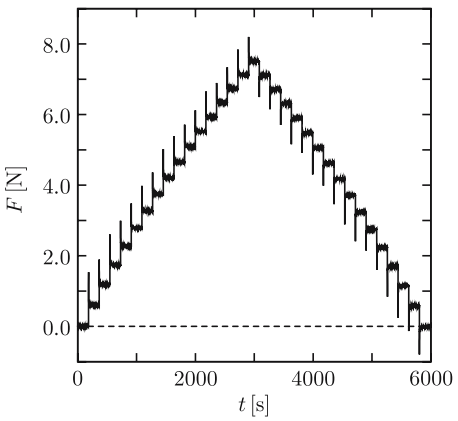

Fig. 8 Measured force during discontinuous tensile test

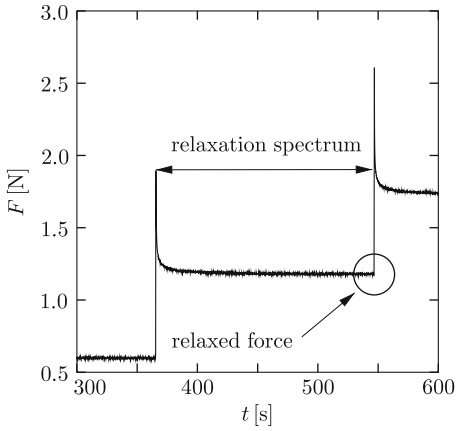

Fig. 9 Magnification of a relaxation step

Figure 9 depicts just one relaxation step as an example. For practical reasons the relaxation time was set to a maximum of 180 s which yields a non-equilibrium stress below a 3% cut-off as proven in long-running relaxation tests, cf. Fig. 10.

By comparing these step relaxation experiments with a tensile test at constant strain rate, it is shown that a machine velocity of $V = 0.01$ mm/s is slow enough to neglect the viscoelastic effects, cf. Fig. 11. The force-values at the end of each relaxation step, i.e. for the loading and for the corresponding unloading step, are averaged and plotted against the machine displacement. This calculated curve describing the relaxed state of the material is then compared with a continuous tensile test (no stops) at a constant deformation rate in order to show how slow the velocity of the machine displacement must be not to activate viscoelasticity, cf. Fig. 11.

For the analysis of the experimental data, we applied the following procedure: as a first step, we calculated the average of the relaxed force values. Then, the commercial

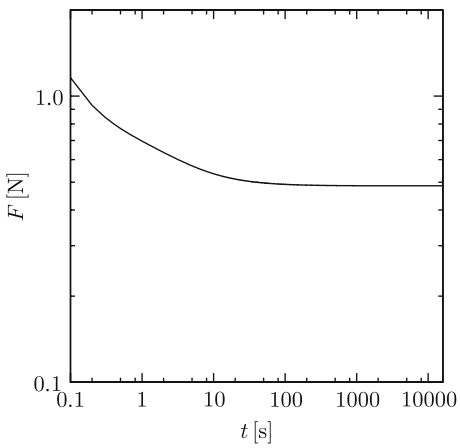

Fig. 10 Long-running relaxation test in a double logarithmic diagram (smoothed)

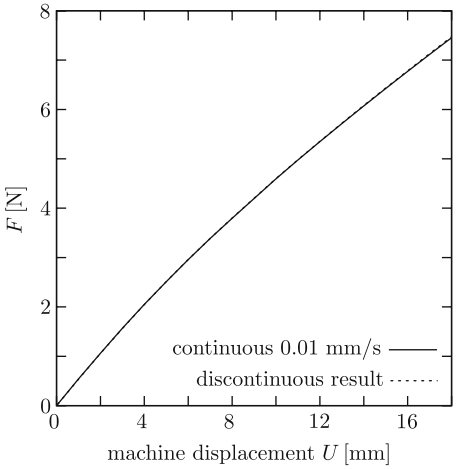

Fig. 11 Comparison between discontinuous and small rate continuous tensile test

NI Vision Development System® software tool is utilised to calculate the stretch λ_1 in $\mathbf{e}_1$-direction via pattern recognition. The stretch λ_1 is given by

$$\lambda_1 = \frac{l}{l_0} \tag{13}$$

where l stands for the distance of two aluminium stripes (Fig. 6) with respect to the current configuration $\mathcal{B}$ (the given level of elongation) and l_0 reflects their distance with respect to the reference configuration $\mathcal{B}_0$ (before loading). Now, the correlation for the component B_{11} of the left Cauchy-Green deformation tensor to the stretch λ_1 is given by

$$B_{11} = \lambda_1^2. \tag{14}$$

Figure 12 presents the evolution of the averaged stretch λ_1 as a function of the machine displacement U for numerous dogbone specimens in the relaxed state as obtained by pattern recognition. A relative error of ±0.322% illustrates the high reproducibility of the measurements.

As the stretch λ_1 is needed not only for discrete points but for the whole machine displacement U we use a linear fit function to describe it (Fig. 12). This linear function

$$\lambda_1 = 1.0 + 0.02632\,\mathrm{mm}^{-1} U \tag{15}$$

has an average error of ±0.256% with respect to the discrete set of experimental data. With Eq. 15 we do not need any further pattern recognition for the viscoelastic experiments.

The same method is used to receive the change in sample width in terms of $\lambda_2 = b/b_0$ with respect to the machine displacement. During the tensile test, we measured the width b of the specimen in detail and set it in

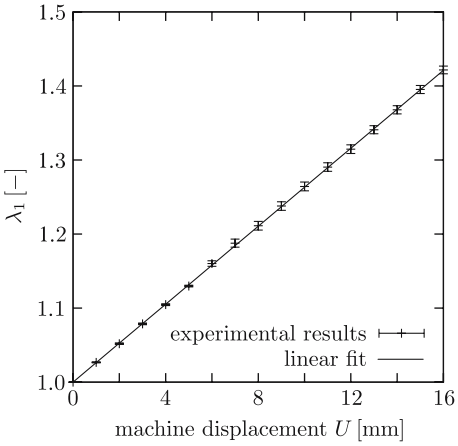

Fig. 12 Stretch λ_1 versus covered machine displacement U and its linear fit

relation to the width b_0 in the undeformed state. The measurement position moved with a traced aluminium stripe. These results are plotted in Fig. 13 and compared with the analytical solution of the incompressibility constraint $\det \mathbf{F} = \lambda_1 \lambda_2^2 = 1$. Herein the implicit basic assumption of isotropy was made, i.e. that the change of the width and of the thickness is the same, $\lambda_2 = \lambda_3$. The comparison between measured and computed data shows that within the margins of experimental error the PUR is incompressible. Henceforth only the analysis of the stretch λ_1 is necessary and the stretch λ_2 in width can be calculated by

$$\lambda_2 = \frac{1}{\sqrt{\lambda_1}}. \tag{16}$$

The cross-section area $A(U)$ of the samples in the current configuration $\mathcal{B}$ is also needed for the calculation of the true stress (Cauchy stress $\mathbf{T}$). It is derived with the above mentioned assumption to

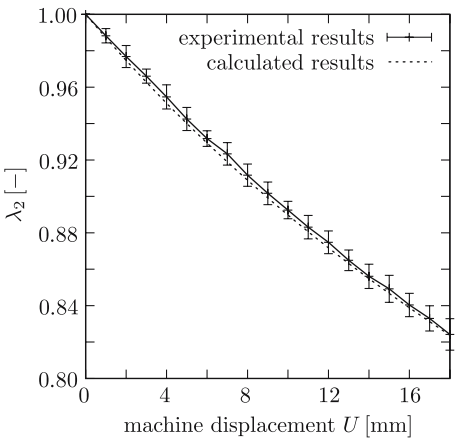

Fig. 13 Analysis of the incompressibility of the material

$$A(U) = A_0\left(\frac{1}{\sqrt{\lambda_1}}\right)^2 = A_0\left(\frac{1}{1.0 + 0.02632U}\right) \tag{17}$$

where A_0 reflects the cross-section area with respect to the reference configuration $\mathcal{B}_0$.

Now the component T_{11} of the Cauchy-stress tensor **T** (true stress) is calculated and plotted against the component B_{11} of the left Cauchy-Green deformation tensor which we get from the solution of Eq. 14. As shown in Fig. 14 for a number of dogbone samples, the experimental stress-deformation curves fall almost together.

With these high-quality data, the model can be aligned to the experiment. In the case of the uniaxial tension test, the analytical solution for the stress-deformation response in the relaxed state is developed out of the Neo-Hookean approach to

$$T_{11} = \mu\left(B_{11} - \frac{1}{\sqrt{B_{11}}}\right) = \mu\left(\lambda_1^2 - \frac{1}{\lambda_1}\right). \tag{18}$$

Here, we take the zero stress in the cross direction into account. The shear modulus μ is determined by the commercial fitting tool Origin Pro®. It has the value of 1.307 ± 0.006 N/mm^2 for over 60 specimens out of different PUR films. Note the superior accuracy. Figure 15 displays the average stress-deformation response and its fit with the Neo-Hookean material model. Again, the model fits extremely well to the data.

Experimental investigation concerning the viscoelastic behaviour of the PUR

For the evaluation of the viscoelastic material parameters uniaxial tension tests with the same dogbone samples at constant strain rates were performed. Tests under loading and unloading conditions were made as shown in Fig. 16.

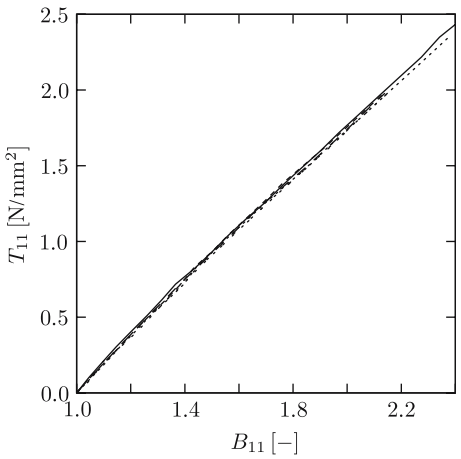

Fig. 14 Stress-deformation diagram of different specimens

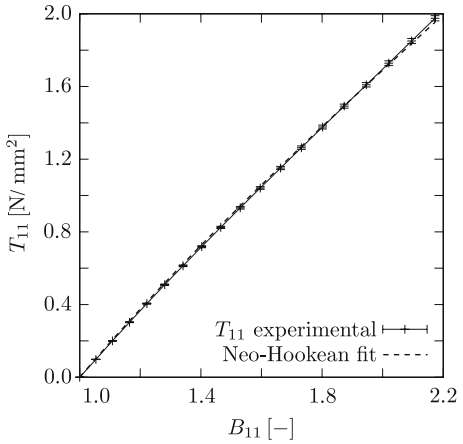

Fig. 15 Experimental average data of true stress T_{11} versus deformation B_{11} and Neo-Hookean fit

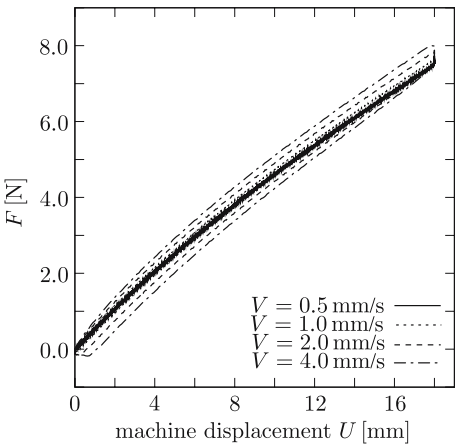

Fig. 16 Force-deformation curves at different rates

We used different machine rates $V = \dot{U}$ and got the associated hysteresis curves for the specimens.

Following the procedure described above, we obtain a set of average loading curves for the stress-deformation response for any constant rate (Fig. 17). The scatter of the rate-dependent material properties is increasing with rising deformation rate but it does not extend the limits of 2–8%.

The non-linear material behaviour depicted in Fig. 17 is much too complex for an analytical solution. Hence, to find the model parameters we use an evolution strategy method which is described in the next chapter.

Parameter identification

Description of the general method

For the identification of the viscoelastic parameters the model response needs to be fitted to the experimental

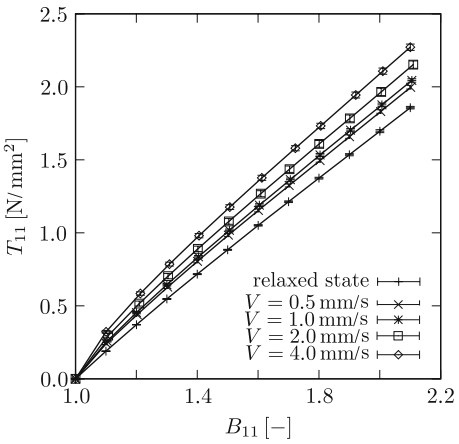

Fig. 17 Experimental average data of true stress T_{11} versus deformation B_{11} at different rates

stress-deformation curves obtained at different rates V. We use a parameter identification strategy combined with a boundary value problem which is solved by finite element analysis. The first goal of our study is to fit qualitatively the model response to the experimental curves by determining the number of Maxwell elements which are required to reproduce the viscoelastic complexity. Secondly, a satisfying quantitative fitting has to be obtained for the values of the parameters μ_e^j and r^j.

From the mathematical point of view the process of parameter identification represents an optimisation problem. In the present study the vector of material parameters $\boldsymbol{\kappa} := \{\mu_e^j, r^j\}$ has to be modified until a good match between experimental data and the prediction of the numerical model is achieved. For that reason a distance function $f(\boldsymbol{\kappa})$ of least squares type, which represents the quality of the approximation between the model response using the parameter vector $\boldsymbol{\kappa}$ and experimental data, has to be minimised. Mathematically this can be formulated as follows: Find $\boldsymbol{\kappa}$ so that

$$f(\boldsymbol{\kappa}) := ||\mathsf{T}(\boldsymbol{\kappa}) - \mathsf{M}(\mathsf{T}^{exp})|| \longrightarrow \text{MIN} \tag{19}$$

see [49]. Herein

$$\mathsf{T}^{exp} = [T_{11}^{\bar{t}_1,exp}, T_{11}^{\bar{t}_2,exp}, \ldots]^T \tag{20}$$

denotes the response variables which are recorded as output from the experiment and

$$\mathsf{T} = [T_{11}^{t_1}, T_{11}^{t_2}, \ldots]^T \tag{21}$$

is calculated from the presented model by finite element analysis. As the problem is homogeneous, we only use one element and solve it at the integration point. In a further step the identification of the model will be done for inhomogeneous experiments. Therefore, the required frame was prepared for the general case. Of course, the accuracy can be increased by time adaptive schemes, e.g. Diebels and Ellsiepen [13] and Ellsiepen and Hartmann [16].

A direct comparison between experimental and calculated results would not be meaningful from a computational point of view especially if time adaptive schemes are used, e.g. [13, 16]. For that reason we introduce the projection operator M which allows the interpolation of the experimental results by

$$\bar{\mathsf{T}}^{exp} = \mathsf{M}(\mathsf{T}^{exp}) \tag{22}$$

with

$$\bar{\mathsf{T}}^{exp} = [T_{11}^{t_1,exp}, T_{11}^{t_2,exp}, \ldots]^T. \tag{23}$$

Figure 18 gives a schematic overview of the applied procedure with respect to the parameter identification. Several strategies have been developed for the approach to solve that class of problems. In general, the strategies can be divided in deterministic and stochastic methods. Both types of strategies require a starting vector $\boldsymbol{\kappa}_0$. In deterministic methods a new parameter vector is calculated using information from the gradient of the objective function at the current vector $\boldsymbol{\kappa}$. The advantage of this strategy is a good and fast convergence if applied to continuous functions. However the calculation of the gradient of the objective function can be troublesome for some constitutive models and a further drawback is the restricted ability to distinguish local and global minima. For details of the application of deterministic strategies, see e.g. [33].

These problems are avoided by the stochastic optimisation method which is based on principles of biological evolution, as it was first introduced by Rechenberg [42] and Schwefel [50]. In our work such a multimembered evolution strategy is employed and the concept behind this method is now shortly explained. Selecting different

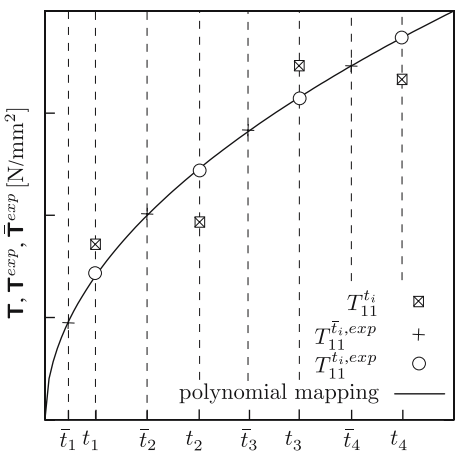

Fig. 18 Schematic overview of the utilised procedure

starting parameter vectors (*parents*), new vectors (*descendants*) are generated from the parents by random mutations, where the step size controls the length of the random changes. The question how to choose the step size is one very important part of the algorithm and is furthermore closely linked to the convergence behaviour. In order to make the algorithm efficient it is suggested that the step size should be modified during the minimum search, cf. [50]. Besides the mutation procedure the mechanism of recombination is used in order to generate additional descendant parameter vectors. For each component of the descendant's parameter vector another parent is randomly selected from the entire parent population. Afterwards the boundary value problem is evaluated for the descendants, where the vectors with the best objective functions are selected to be the parents of the next generation. There are various publications like [17, 39] where the evolutionary algorithm has been proved as a robust optimisation technique which can be used as a *Black Box* algorithm for different classes of material models.

Numerical results

In this section, we present numerical results obtained with the identification procedure described above. We use the mean stress-deformation curves at four different machine rates V ranging from 0.5 to 4.0 mm/s to identify the material parameters. It should be mentioned that the shear modulus μ which characterises the equilibrium elastic material behaviour was set to 1.307 N/mm^2 as identified from the uniaxial relaxation tests. The first step of our investigation concerns the number of Maxwell elements which are required to describe the non-linear viscoelastic behaviour of the polyurethane. We repeat the parameter identification for different numbers of Maxwell elements, following an empirical rule, which divides the relaxation spectrum of the material into time decades, where each decade can be represented with one or more Maxwell elements. According to our experimental results we expect the values of the relaxation parameters to be in the following intervals 0–1 s, 1–10 s and 10–100 s. The simultaneous adjustment of the slowest (0.5 mm/s) and the fastest (4.0 mm/s) rate has shown that four Maxwell elements are required for a satisfactory description of the non-linear relaxation behaviour. Each Maxwell element is described by two parameters, μ_e^j and r^j, so that in total eight parameters have to be identified by minimising the least squares error over all four rates, Eq. 19. In detail, three parent vectors were used in each generation. For the first generation they were randomly chosen within the feasible search domain, and for the next iterations the ones with the best objective function were qualified as parents. Within one generation three new vectors were generated from each parent vector by random mutation and four additional vectors were created by recombination of the total twelve vectors. That means that per generation the objective function was evaluated sixteen times, and only the vectors with the lowest least squares function values were used for the next generation.

Table 1 Identified pure elastic and viscoelastic material parameters with μ, μ_e^j in [N/mm^2] and r^j in [s]

μ	μ_e^1	μ_e^2	μ_e^3	μ_e^4
1.307	0.801	0.199	0.441	0.081
–	r^1	r^2	r^3	r^4
–	0.226	0.529	3.312	97.998

The minimum was reached after 400 iterations. The optimised set of material parameters $\boldsymbol{\kappa}$ is listed in Table 1. It can be seen that the values of the identified relaxation times (r^1–r^4) agree with our expectations according to the relaxation spectrum.

The good correspondence between experimental data and the model prediction using the parameters identified in the present study is shown in Fig. 19. Here, the component T_{11} of the stress tensor $\mathbf{T}$ is plotted over the component B_{11} of the left Cauchy-Green deformation tensor with the corresponding error bars for all strain rates. Note, that for each rate V the simulated curve lies within the error bars, i.e. the obtained parameters satisfactorily describe the viscoelastic behaviour of our polyurethane within the investigated range of machine rates.

Cyclic tests at different strain rates show significant variations between the simulated and experimentally observed stress-deformation responses at the end of unloading due to the tensile specimens which do not qualify for pressure, cf. Figs. 20–23.

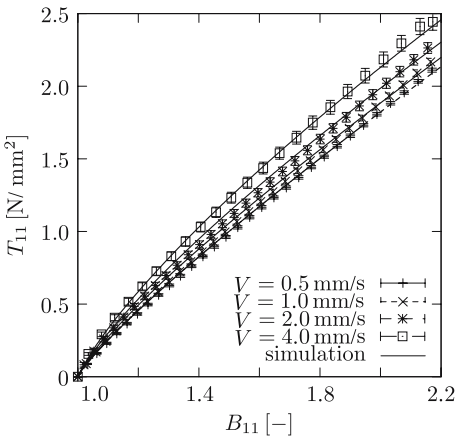

Fig. 19 Comparison of experimental and numerical stress-deformation curves for the tensile test of PUR dogbone specimens

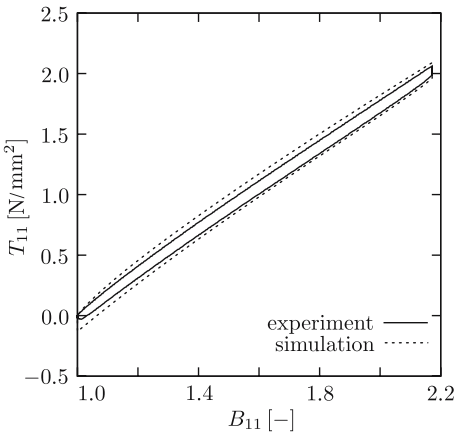

Fig. 20 Comparison of experimental and numerical stress-deformation curves for cyclic tests for a deformation velocity of 0.5 mm/s

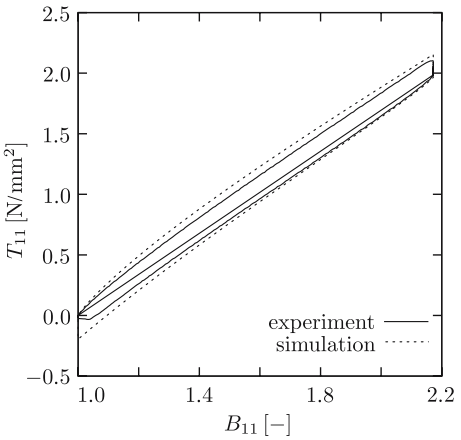

Fig. 21 Comparison of experimental and numerical stress-deformation curves for cyclic tests for a deformation velocity of 1.0 mm/s

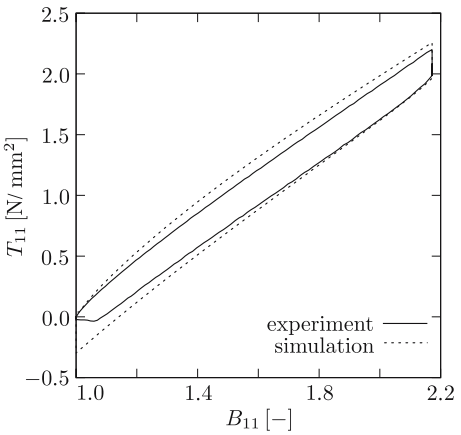

Fig. 22 Comparison of experimental and numerical stress-deformation curves for cyclic tests for a deformation velocity of 2.0 mm/s

Figure 24 shows the numerical simulation of a relaxation experiment in comparison to the obtained experimental results. The set of parameters determined

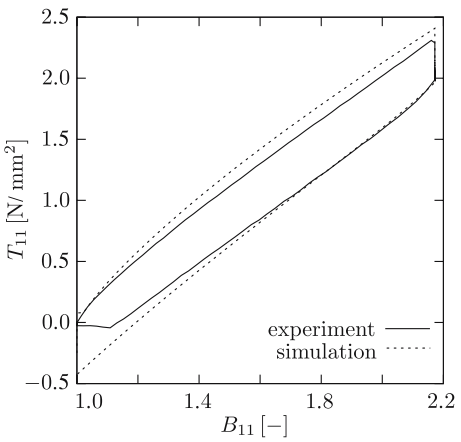

Fig. 23 Comparison of experimental and numerical stress-deformation curves for cyclic tests for a deformation velocity of 4.0 mm/s

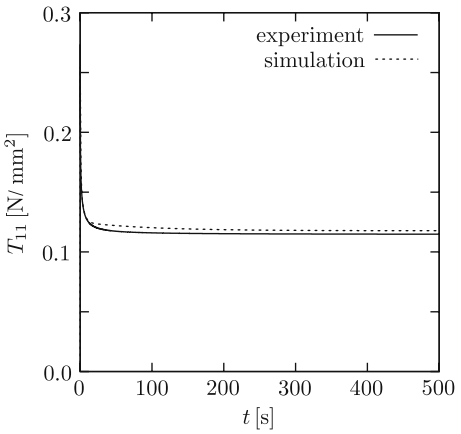

Fig. 24 Comparison of experimental and numerical stress-relaxation curves for a time of 500 s

from uniaxial tension tests at constant strain rates allow to simulate the relaxation behaviour of the PUR in good agreement with the experiments. Only the stress-peak at the beginning of the experiment and the stress response in the relaxed state show very small differences. Nevertheless, one can say that the material parameters obtained from the uniaxial tension test at constant strain rates are able to simulate quite well the performance in other experiments which were not used for the identification procedure.

Conclusion and discussion

This paper combines experimental investigations and theoretical modelling of an elastomer PUR network from the sample preparation to the development of the simulation tools. As a result, the polyurethane is proven to be an incompressible viscoelastic material (no plasticity, no

damage effects, no volumetrical extension) in the investigated range of deformation. The aspects of finite linear viscoelasticity are combined with the Neo-Hookean material model. The material parameters of the model are determined by a biological evolution strategy method. This is done on the basis of the high quality experimental data by solving the boundary value problem by finite element analysis.

A comparison of the model predictions using the obtained parameters shows an excellent agreement with the set of experiments. The model results lie within the experimental scatter. Since the presented model adaption is based on uniaxial data, the material behaviour will be checked by additional experimental investigations (e.g. shear or torsion tests and biaxial experiments). Additionally, the model verification should be completed by measurements with higher deformation rates and by inhomogeneous experiments. In order to reduce the number of material parameters for practical applications, a non-linear evolution equation will be formulated for the internal variables.

Acknowledgements The authors are grateful to the DFG (German Science Foundation—Deutsche Forschungsgemeinschaft) for financial support through the grant numbers Di 430/5-1 and Po 577/15-1.

References

1. Amin AFMS, Alam MS, Okui Y (2002) Mech Mater 34:75
2. Amin AFMS, Alam MS, Okui Y (2003) J Test Eval 31(6):524
3. Amin AFMS, Lion A, Sekita S, Okui Y (2006) Int J Plasticity 22:1610
4. Batal J (2002) Möglichkeiten zur Messung der Haftkraft einer strukturierten Polymeroberfläche. Universität des Saarlandes, Saarbrücken
5. Batal J (2004) Haftkraftmessung an biomimetisch strukturierten Polymeroberflächen. Universität des Saarlandes, Saarbrücken
6. Braess D (1997) Finite Elemente. Springer, Berlin
7. Bergstrom JS, Boyce MC (1998) J Mech Phys Solids 56(5):931
8. Boyce MC, Arruda EM (2000) Rubber Chem Technol 73:504
9. Bergstrom JS, Boyce MC (2000) Mech Mater 32:627
10. Bergstrom JS, Boyce MC (2001) Macromolecules 34(3):614
11. Bergstrom JS, Boyce MC (2001) Mech Mater 33:523
12. Coleman B, Noll W (1963) Arch Ration Mech Anal 13:167
13. Diebels S, Ellsiepen P, Ehlers W (1999) Tech Mech 19:19
14. Dzierza W (1978) J Appl Polym Sci 22:1331
15. Ehlers W, Ellsiepen P, PANDAS: Ein FE-System zur Simulation von Sonderproblemen der Bodenmechanik. Ernst & Sohn, Berlin 1998, p 400
16. Ellsiepen P, Hartmann S (2001) Int J Numer Meth Eng 51:679
17. Furukawa T, Yagawa G (1997) Int J Numer Meth Eng 40:1071
18. Haupt P (2000) Continuum mechanics and theory of materials. Springer, Berlin
19. Haupt P, Lion A, Backhaus E (2000) Int J Solids Struct 37:3633
20. Haupt P, Lion A (2002) Acta Mech 159:87
21. Khan AS, Lopez-Pamies O, Kazmi R (2006) Int J Plasticity 22:581
22. Keck J (1998) Zur Beschreibung finiter Deformationen von Polymeren, Experimente, Modellbildung, Parameteridentifikation und Finite-Elemente-Formulierung. Bericht-Nr. I-5 des Instituts für Mechanik (Bauwesen), Stuttgart
23. Kröner E (1960) Arch Ration Mech Anal 4:273
24. Laiarinandrasana L, Piques R, Robisson A (2003) Int J Plasticity 19:977
25. Lee EH, Liu DT (1967) J Appl Phys 38:19
26. Lee EH (1969) J Appl Mech 36:1
27. Leterrier Y, G'sell C (1988) J Mater Sci 23:4209
28. Lion A (1996) Continuum Mech Therm 8:153
29. Lion A (1997) Acta Mech 123:1
30. Lion A (1999) Rubber Chem Technol 72: 410
31. Lion A, Thermomechanik von Elastomeren. Bericht-Nr. 1/2000 des Instituts für Mechanik, Kassel 2000
32. Lubliner J (1985) Mech Res Commun 12:93
33. Mahnken R (1996) Int J Plasticity 12:451
34. Miehe C, Keck J (2000) J Mech Phys Solids 48:323
35. Miehe C, Göktepe S, Lulei F (2004) J Mech Phys Solids 52:2617
36. Miehe C, Göktepe S (2005) J Mech Phys Solids 53:2231
37. Göktepe S, Miehe C (2005) J Mech Phys Solids 53:2259
38. Mooney M (1940) J Appl Phys 11:582
39. Müller D, Hartmann G (1989) J Eng Mater Technol 111:299
40. Partom Y (1983) Polym Eng Sci 23:849
41. Randrianantoandro H, Nicolai T, Duront D, Prochazka F (1997) Macromolecules 30:5893
42. Rechenberg I (1973) Evolutionsstrategie: optimierung technischer Systeme nach Prinzipien der biologischen Evolution. Frommann-Holzboog, Stuttgart
43. Reese S (2001) Thermomechanische Modellierung gummiartiger Polymerstrukturen. F01/4 Institut für Baumechanik und Numerische Mechanik, Hannover
44. Reese S, Govindjee S (1998) Mech Time-Depend Mater 1:357
45. Reese S, Govindjee S (1998) Int J Solids Struct 35:3455
46. Reese S, Wriggers P (1997) Comput Methods Appl Mech Eng 148:279
47. Reese S, Wriggers P (1999) In: Dorfmann A, Muhr A (eds) Modelling of the thermomechanical material behaviour of rubber-like polymers–micromechanical motivation and numerical simulation. Proceedings of the First European Conference on Constitutive Models for Rubber, Rotterdam, p 13
48. Rivlin RS (1947) Phil Trans R Soc Lond A 241:379
49. Scheday G, Theorie und Numerik der Parameteridentifikation von Materialmodellen der finiten Elastizität und Inelastizität auf der Grundlage optischer Feldmessmethoden. Bericht-Nr. I-11 des Instituts für Mechanik (Bauwesen), Stuttgart 2003
50. Schwefel HP (1995) Evolution and optimum seeking. Wiley, New York
51. Tallec PL, Kaiss A, Rahier C (1994) Int J Numer Meth Eng 37:1159
52. Treloar LR (1976) Proc R Soc Lond A 351:301